

Multi feature-rich synthetic colour to improve human visual perception of point clouds

Jesús Balado^{*}, Elena González, Juan L. Rodríguez-Somoza, Pedro Arias

CINTECX, Universidade de Vigo, GeoTECH Group, 36310 Vigo, Spain

ARTICLE INFO

Keywords:

LiDAR
CIELAB
Mobile laser scanning
Mobile mapping systems
Quality assessment
Point clouds

ABSTRACT

Although point features have shown their usefulness in classification with Machine Learning, point cloud visualization enhancement methods focus mainly on lighting. The visualization of point features helps to improve the perception of the 3D environment. This paper proposes Multi Feature-Rich Synthetic Colour (MFRSC) as an alternative non-photorealistic colour approach of natural-coloured point clouds. The method is based on the selection of nine features (reflectance, return number, inclination, depth, height, point density, linearity, planarity, and scattering) associated with five human perception descriptors (edges, texture, shape, size, depth, orientation). The features are reduced to fit the RGB display channels. All feature permutations are analysed according to colour distance with the natural-coloured point cloud and Image Quality Assessment. As a result, the selected feature permutations allow a clear visualization of the scene's rendering objects, highlighting edges, planes, and volumetric objects. MFRSC effectively replaces natural colour, even with less distorted visualization according to BRISQUE, NIQE and PIQE. In addition, the assignment of features in RGB channels enables the use of MFRSC in software that does not support colorization based on point attributes (most commercially available software). MFRSC can be combined with other non-photorealistic techniques such as Eye-Dome Lighting or Ambient Occlusion.

1. Introduction

The difficult visualisation is one of the main limitations of point clouds. There are several causes that hinder the visualization (Burwell et al., 2012; Richter and Döllner, 2014; Meynet et al., 2019): 3D perspective, surface overlaps, occlusions, rendering of large numbers of points, excessive level of detail, and sometimes, the absence of natural colour. Although point clouds obtained by photogrammetric techniques have natural colour associated with each point, LiDAR technology does not acquire colour from the environment (Abdelhafiz, 2013), instead the colour must be acquired independently using a camera, and the photographs must be projected onto the point cloud for colouring each point with a pixel value (Spehr et al., 2010). This process is not perfect and leads to a number of colouring errors (González et al., 2022).

In remote sensing, colour/hue is the main visual criteria for image interpretation and object detection, followed by size, shape, texture, patterns, height, shadow, site, and association (Estes et al., 1983). According to the Gestalt principle of similarity, the human eye tends to group similar objects, including similarity of colour (Chiu et al., 2017;

Quinlan and Wilton, 1998; O'Connor, 2015). Furthermore, in the process of visual perception, edges of the objects are first detected and then the stereoscopic process is performed (Oliva and Pérez-Sust, 2008), adding texture, depth and orientation, capturing movement and colour.

When the point cloud has not been coloured, the interpretation of the environment is more difficult, the edges cannot be clearly identified either, and a colour band visualisation is often used according to reflectivity (to distinguish textures) or height (to identify the verticality of the environment) (Otepka et al., 2020). However, although scarce for the human eye, point cloud features are very useful for the identification of objects by Artificial Intelligence. In recent years, many authors have extracted features from points clouds, achieving very high success rates in point and object classification (Weinmann et al., 2015; Soillán et al., 2020; Li and Cheng, 2018; Özdemir et al., 2019). Geometric features (linearity, planarity, sphericity, omnivariance, anisotropy, eigenentropy, sum of eigenvalues, and change of curvature) are the most employed in classification, but other type of features (Z-related, radiometric, shape, contextual and multiple segmentations) have also shown their usefulness (Golovinskiy et al., 2009). A large number of features

^{*} Corresponding author.

E-mail address: jbaloado@uvigo.es (J. Balado).

<https://doi.org/10.1016/j.isprsjprs.2023.01.019>

Received 15 August 2022; Received in revised form 17 January 2023; Accepted 25 January 2023

Available online 31 January 2023

0924-2716/© 2023 The Author(s). Published by Elsevier B.V. on behalf of International Society for Photogrammetry and Remote Sensing, Inc. (ISPRS). This is an open access article under the CC BY license (<http://creativecommons.org/licenses/by/4.0/>).

also does not ensure a better classification and often leads to overfitting (Weinmann and Weinmann, 2019).

The aim of this paper is to combine nine features to generate synthetic colour attributes that improve human perception of point clouds and object recognition as close as possible to the natural colour. Following the currently employed Young-Helmholtz trichromatic colour theory (Wade, 2021), the nine features are distributed over the three RGB channels (after 9–3 reduction process). Furthermore, all possible permutations of features per channel are tested to ensure maximum proximity to the natural colour and quality of the resulting images. The most relevant contributions of this paper are:

- Selection of nine features based on geometry and visual perception criteria: reflectance, return number, inclination, depth, height, point density, linearity, planarity, and scattering.
- Application of seven Image Quality Assessment metrics for the evaluation of the raster images generated from the point cloud.
- Calculation of the colour distance between synthetic-coloured and natural-coloured point clouds in the CIELAB colour space.
- Analysis of the 362,880 permutations generated from the nine features and recommendation of the highest quality combinations.
- Tests on one point cloud acquired with a Mobile Mapping System in a real urban environment with built and green elements.

The reminder of this paper is structured as follows. In Section 2, works on point cloud visualization and Quality Assessment are compiled. The proposed method is explained in Section 3. Section 4 is dedicated to present and analyse the results. The discussion in Sections 5 and 6 concludes this paper.

2. Related work

2.1. Point cloud visualization

Point cloud visualization has had less research compared to automatic point cloud processing and feature extraction (Uchida et al., 2020). From the beginning, there have been two trends in visualization: point-based and mesh-based rendering techniques. The best results of point-based techniques rendering are obtained when each point is replaced with an oriented flat circular disk whereas the orientations and the radii of such disks can be estimated from the point cloud data (Aliev et al., 2020). Advocates of point-based rendering techniques argue that this visualization is closer to the scanned data and allows a better interpretation, avoiding the omission of small details caused by modelling workflows (Virtanen et al., 2020). The main limitation of point-based rendering techniques is the inability to represent linear edges caused by missing data between points, which leads to “see through” the surface. Creating realistic 3D models, e.g., meshes (shaded or texturized), helps to visualize the final result much better than a wireframe representation (Remondino, 2003). Usually, mesh-based rendering techniques require per-point attributes such as surface normals, local point densities, colours, and object class information, typically computed in pre-processing (Richter and Döllner, 2014), so their existence is assumed (Richter and Döllner, 2010).

After the introduction of web graphic library (WebGL), powered by HTML5 (Vahid and Wang, 2019), several web renderers have become available, complementing desktop-based solutions. At that time, one of the major limitations of real-time point cloud visualization became apparent: their massive size. The term massive point clouds encompass all point clouds that require big data solutions for storage, management, analysis, processing, dissemination, and visualization (van Oosterom et al., 2015). Point clouds contain more and more information (Richter and Döllner, 2014), both in terms of number of points, which can reach several billions, and in terms of attributes. Since the available hardware resources of CPU and GPU are limited, and massive point clouds exceed available memory size (Richter and Döllner, 2010), the visualization

relies on hierarchical acceleration structures (Schütz et al., 2020; Martínez Rubi et al., 2015; Discher et al., 2019): regular grids (Yang and Huang, 2014), quadrees (Nelson et al., 2015), octrees (Schütz et al., 2020), KD-trees (Wang et al., 2021), multiple Level of Detail (LoD) (Liu et al., 2020), or Hierarchically Layered Tiles (HLT) (Deibe et al., 2019). Other alternatives are the reduction of the number of points (considering the loss of information), and distributed computing (Hieu et al., 2022).

The release of game graphic engines, such as Unity (Hofer et al., 2018) or Unreal (Edler et al., 2020), for 3D object visualization also made an important contribution to point cloud visualization. Game engine-based point cloud visualization has advantages in pre-processing and rendering efficiency, detail level, and volume perception (Liu et al., 2021), allowing interactions between the user and the point cloud (Virtanen et al., 2020). In addition, the arrival of eXtended Reality devices on the market also brings specific challenges in point cloud visualization. In Augmented Reality (Wang et al., 2019; Placitelli and Gallo, 2011; Zhang et al., 2020), it is necessary lightness adjustment for regions with similar colours of the point cloud and the background, and colour enhancement for regions with fewer projected points (Li et al., 2019). Virtual Reality (Vincke et al., 2019) needs a high FPS rate (Discher et al., 2018) and realistic objects (Alexiou et al., 2019).

To improve the visualization of point clouds, there are photorealistic and non-photorealistic post-processing techniques. Photorealistic techniques aim at a visualization closer to the real world by applying appropriate point size, orientation, textures, and colour schemes. Non-photorealistic techniques deal with the fuzziness of a 3D point cloud and highlight edges and structures (Discher et al., 2019). A very common technique is the EDL (Eye-Dome Lighting), consisting of lighting group of points close and shading their outlines, which accentuates the shapes of objects (Boucheny and Ribes, 2011) and facilitate visual filtering (Discher et al., 2018). Another widespread technique is Ambient Occlusion (AO), lighting model that approximates the diffuse illumination of surfaces based on the directly visible occluders (Bavoil and Sainz, 2009; Shi et al., 2022). Artificial Intelligence has even been proposed to generate non-photorealistic rendering techniques (Zhang et al., 2020; Ren and Song, 2022). In addition, Uchida et al. (2020) propose a transparent visualization of point clouds to reduce the noise.

Several authors have concluded that the use of features offers additional information for visualization. In Otepka et al. (2020), the authors indicate that planarity is useful for identifying planar regions, NormalizedZ for height above terrain, EchoRatio for vertical penetration measure and NormalSigma0 for detecting smooth or rough areas. In Aliev et al. (2020), the proposed system learns the neural descriptors for every point (e.g. Principal Component Analysis dimensions) and the neural rendering network maps the rasterized point descriptors to realistic images. However, vast amount of software available for point cloud visualization allow visualization by RGB, but only CloudCompare, opalsView and Potree support colorization based on point attributes (Otepka et al., 2020).

Regarding to previous approaches, in this work a non-photorealistic technique based on the simultaneous visualization of nine point cloud features is presented. To the best of the author's knowledge, this combination of features has not been proposed before. Nine feature combination improves point cloud interpretation through synthetic colour, and it can be implemented in any software that support point cloud rendering with RGB information.

2.2. Point cloud quality Assessment (PCQA)

Point clouds are a very useful data type for 3D visualization and immersive experiences. Given the high file transfer rate in multimedia applications, new MPEG standards are being applied to point clouds (Schwarz et al., 2019). The compression methods imply information loss, that typically leads to degradation of the visual quality and, therefore, which can affect the user experience (Alexiou and Ebrahimi, 2019), so many authors have designed new Point Cloud Quality

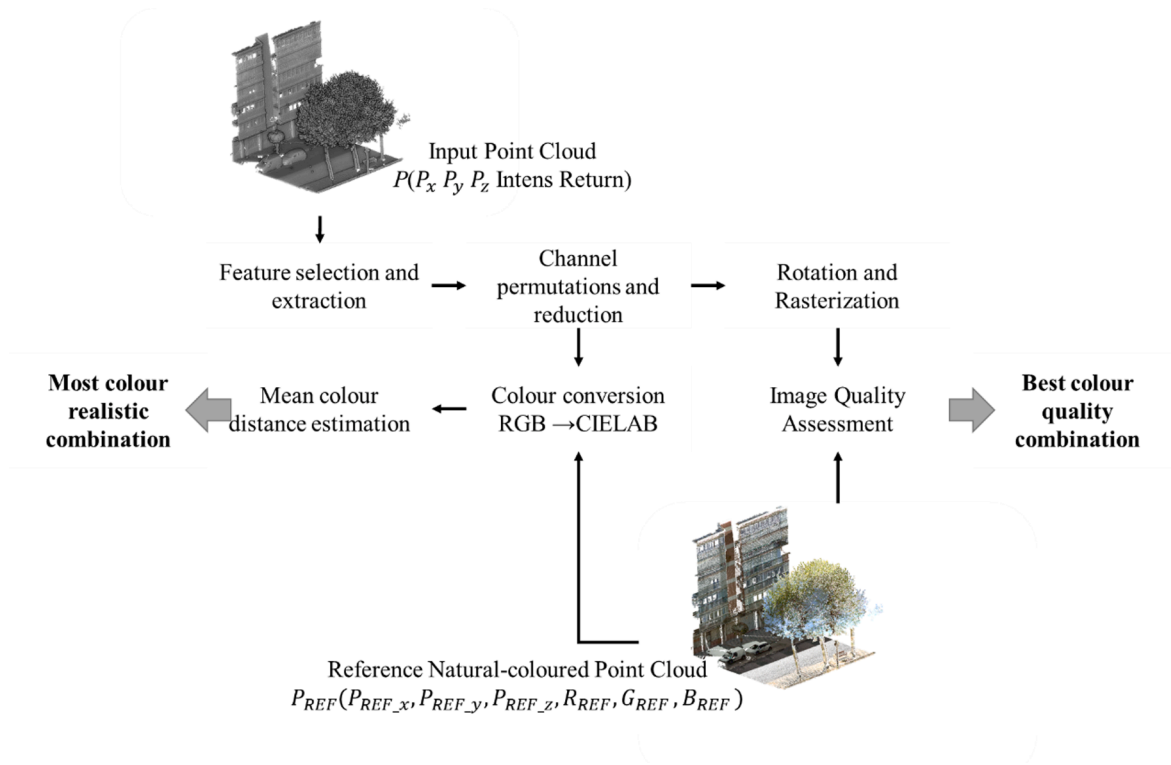


Fig. 1. Workflow of the methodology.

Assessment (PCQA) methods. Although QA was already widely used in image processing, point clouds pose a new challenge due to the unstructured and non-uniformly distributed points. The objective of QA methods is to have a correlated evaluation of human quality assessment and human perception (Javaheri et al., 2017); the scores obtained are very subjective. Specifically, PCQA methods evaluate both the geometry and radiometry (colour-textures) of the point cloud through reference data (Viola et al., 2020).

Colour-texture are evaluated in a similar way to image processing metrics. They are also based on neighbourhood relations between points, and calculation of colour distances. In Diniz et al. (2021), Perceptual Colour Distance Patterns are presented considering a local neighbourhood for the computation and colour distances based on CIELAB colour-space. In Diniz et al. (2020), Local Binary Pattern (LBP) descriptor is adapted to point clouds considering the nearest points as the neighbourhood pixels of the descriptor. In Diniz et al. (2020), the LBP neighbourhood pixels are based in a voxel distribution.

Subjective and objective evaluations are critical in order to assess the visual quality of media content (Alexiou and Ebrahimi, 2017), but despite the progress made, there is a consensus that PCQA is an open problem (Diniz et al., 2020). In this work, PCQA is evaluated through point cloud rasterization (3D to 2D projection) in an isometric view, similar to that presented in Torlig et al. (2018). This option has been selected for the following reasons:

- No changes are performed that affect the geometry of the point cloud; therefore, it is not necessary to evaluate the geometric quality of the results.
- QA on images is more developed than on point clouds (many PCQA proposals have been adapted from image processing to point cloud processing) and the objective of this work is not to propose a new PCQA.
- Although point clouds are 3D information, human visualization continues to be by 2D multi-views.

3. Methodology

The proposed method to improve the visualisation of point clouds and to replace the natural colour by a Multi Feature-Rich Synthetic Colour (MFRSC) is explained in this section. It is based on the selection and extraction of nine features from the input point cloud $P(P_x, P_y, P_z, \text{Intens}, \text{Return})$: reflectance, return number, inclination, depth, height, point density, linearity, planarity, and scattering. The order of combination of these nine features influences the quality and realism of the scene. In order to select the most realistic colour combination, the colour distance is calculated through the conversion from RGB to CIELAB space. To evaluate the quality of the visualisation, seven Image Quality Assessment metrics (MSE, PSNR, SSIM, CSV, BRISQUE, NIQE, PIQE) are applied to raster images generated from point clouds. Fig. 1 shows the workflow.

3.1. Feature selection and extraction

Many features are highly dependent on the type of LiDAR used for the survey and the environment. In addition, some features can be expensive to calculate (in terms of computation time or completeness), and often, point cloud features are interdependent on each other.

Some of the features require previous k nearest neighbourhood search and eigenvalue calculations. The eigenvalues represent the extent of a 3D ellipsoid along the principal axes of the k nearest points to each point P_i (Weinmann et al., 2015). The eigenvalues are calculated from the covariance (Eq. (1)) where \bar{P} is geometric centre of the neighbourhood of P_i (Eq. (2)). If there is a vector V in $\mathbb{R}^3 \neq 0$ such $SV = \lambda V$, then the eigenvalues are $\lambda_1 \geq \lambda_2 \geq \lambda_3 \geq 0$. The selected features must be aligned with key perceptual descriptors that facilitate visual recognition.

$$S = \frac{1}{k+1} \sum_{i=0}^k (P_i - \bar{P})(P_i - \bar{P})^T \quad (1)$$

Table 1

Relation between point cloud selected features and perceptual descriptors.

Point cloud features Perception descriptor	Edges	Texture	Shape	Size	Depth	Orientation
Reflectance		x				x
Return number		x				
Inclination			x			x
Depth	x			x	x	x
Height	x			x	x	x
Point density	x	x				
Linearity	x		x			
Planarity	x		x			
Scattering	x		x			

$$\bar{P} = \frac{1}{k+1} \sum_{i=0}^k P_i \quad (2)$$

In view of the above, the nine features used in this work are proposed and justified below:

3.1.1. Reflectance (Re)

The reflectance intensity (Re) is a radiometric feature provided by the LiDAR sensor. According to Höfle and Pfeifer (2007), the reflectance depends on a reference range, the distance between the laser scanner and the object, the angle of incidence, the instrument, and atmospheric conditions. Despite its high variability and dependence on the above mentioned factors, reflectivity is a widely used feature to identify surfaces (Colomb et al., 2019), mainly with high reflectivity such as road markings and traffic signs (Guan et al., 2018), as well as to preserve textures due to variations in material and roughness (Mourño et al., 2021).

3.1.2. Return number (Rn)

Return number (Rn) is a radiometric characteristic related to the penetration capacity of the laser in vegetation elements and crystals

according to their wavelength. Return number feature is only available in multi-return LiDAR and the maximum number of returns is usually five for new LiDAR systems (Nik Effendi et al., 2021). This feature is widely used in the identification of vegetation cover (Ekhtari et al., 2018; Ali et al., 2021) and in less extent, glass windows (Zhang and Zakhori, 2014).

3.1.3. Inclination (In)

Inclination (In) is the feature that indicates the orientation of the surface containing the point with respect to the horizon. The inclination is obtained from the calculation of the surface normal $N(N_x, N_y, N_z)$ of the point regarding to k nearest neighbours (Eq. (3)). The first feature-based recognition model, known as the *pandemonium* proposed by Selfridge (1988), envisages that the visual system can have detectors of simple geometric features such as vertical, horizontal and oblique lines. Therefore, the visualisation of the inclination of surfaces in the point cloud can help in a more direct recognition.

$$inclination = \left| \arctan \left(\frac{\sqrt{N_x^2 + N_y^2}}{N_z} \right) \right| \quad (3)$$

Table 2

Channel permutation sorted by MCD.

Channel permutation (feature order)	MCD
HeLiPIRnReInDeScPd	44.47
RnReInDeScPdHeLiPI	44.49
DeLiRnHeRePdPlScIn	44.52
RnLiDeHeRePdPlScIn	44.55
RnLiDePlScInReHePd	44.65
...	
HeRnDeInPdPIReScLi	87.52
RnHeDeInPdPlScReLi	87.54
RnInHePlPdDeScReLi	87.73
HeRnDeInPdPlScReLi	87.81
HeInRnPlPdDeScReLi	87.81

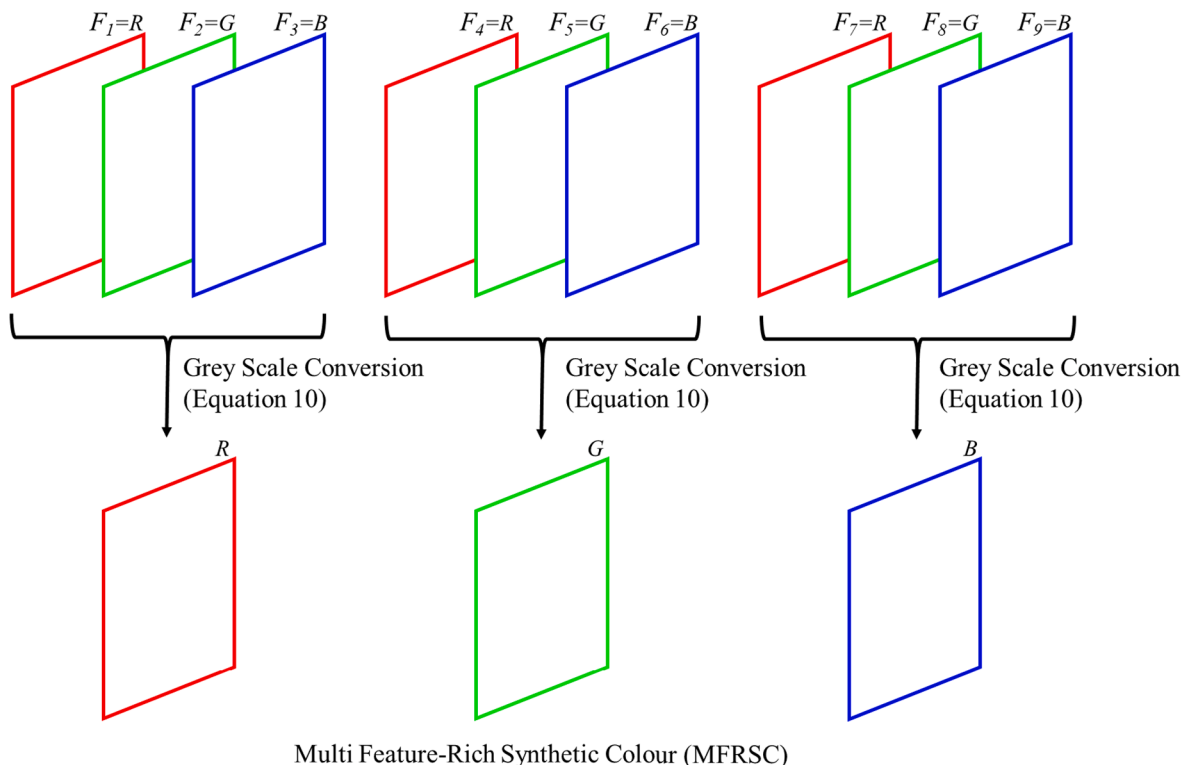
**Fig. 2.** Schematic diagram of the feature distribution according to their order in the RGB colour channels.

Table 3

Channel permutation sorted by IQA metrics with reference.

Feature order MSE		Feature order PSNR		Feature order SSIM		Feature order CSV	
PLiHeDeRnRePdScIn	2068	HeInRnScReLiPiPdDe	10.87	HeDeLiScReRnInPdPl	0.3906	DePdRnScReHePlInLi	0.9205
DeRnRePLiHePdScIn	2081	HeInLiScReRnPiPdDe	10.92	LiDeHeScReRnInPdPl	0.3907	DePdRnScReLiPiInHe	0.9205
PLiInDeRnRePdScHe	2097	HeInRnScReLiPdPiDe	10.93	DeHeLiScReRnInPdPl	0.3923	RnPdDeScReHePlInLi	0.9205
PdScInDeRnRePLiHe	2100	HeInRnReScLiPiPdDe	10.94	HeDeLiReScRnInPdPl	0.3926	PlInRnScReHeDePdLi	0.9205
PLiInHeRnRePdScDe	2102	DeInHeScReLiPiPdRn	10.95	LiDeHeReScRnInPdPl	0.3927	DePdHeScReRnPiInLi	0.9205
...
HeScLiReInRnPiPdDe	4303	PLiInHeRnRePdScDe	14.90	PLiHePdRnInDeScRe	0.5526	ScPiHePdRnReDeLiIn	0.9387
LiScRnHeInRePiPdDe	4330	PdScInDeRnRePLiHe	14.91	PLiHeInRnPdDeScRe	0.5531	ScPiHePdLiInDeRnRe	0.9389
LiScReHeInRnPiPdDe	4334	PLiInDeRnRePdScHe	14.91	PLiInPdHeRnDeScRe	0.5543	ReRnPiPdScInHeLiDe	0.9390
ReScRnHeInLiPiPdDe	4340	DeRnRePLiHePdScIn	14.95	PLiInPdRnHeDeScRe	0.5544	RnLiDePdScInHeRePl	0.9393
ReScLiHeighInRnPiPdDe	4348	PLiHeDeRnRePdScIn	14.97	PLiInHeRnPdDeScRe	0.5560	RnLiPiPdScInHeReDe	0.9395

Table 4

Channel permutation sorted by IQA metrics without reference.

Feature order BRISQUE		Feature order NIQE		Feature order PIQE	
ScPIRnLiDePdInHeRe	34.83	ScRnPdInDePIHeLiRe	9.276	LiPIPdScDeRnReHeIn	40.05
ScPIInLiDePdRnHeRe	34.90	ScInHeRnDeLiPdPIRe	9.315	LiPIRnHeDeScPdReIn	40.14
ScPIInLiDeHeRnPdRe	34.90	ScRnHeInDeLiPdPIRe	9.341	LiScPdPIDeReRnHeIn	40.16
ScLiRnPIDePdInHeRe	34.91	ScInHeRnDePIPdLiRe	9.377	LiScPdPIDeRnReHeIn	40.16
ScLiInPIDePdRnHeRe	34.92	PIRnHeInDeScPdLiRe	9.392	LiScInPIDeHeRnRePd	40.21
...		
PdScHePIReInDeLiRn	47.00	PdLiPIRnReHeDeScIn	15.23	HeReDeRnPIPdScInLi	64.45
PdScHePIReLiInRnDe	47.01	DeLiScRnReHeInPdPI	15.23	DeReScRnPIPdHeInLi	64.45
PdScInPIReLiHeRnDe	47.01	ScLiPIRnReHeDePdIn	15.23	ReRnScPdLiDeInHePI	64.46
RnScPdPIReLiHeInDe	47.01	PdRnDeLiReHePIScIn	15.27	ScRnDeRePIHePdInLi	64.47
PdPIDeScReLiInRnHe	47.02	HeRnPILiRePdInScDe	15.30	DeRnPdRePIHeScInLi	64.61

3.1.4. Depth (De)

Depth (De) is the feature that provides a visualisation of horizontal distances. Depth is a very useful feature to identify objects by their silhouette (difference in distance between target and background). Many 3D cameras base their principle of operation on depth images (3D Object Recognition System, 2019; Tham et al., 2015). In point clouds, depth can be calculated in various ways, with the calculation from the scanning position of the LiDAR being common (Ma et al., 2019, 2018). Since the built environment can take many forms and LiDAR position or MLS trajectory data are not always available, the proposed depth is calculated according to X and Y coordinates (P_x, P_y) (Eq. (4)).

$$depth = \sqrt{P_x^2 + P_y^2} \quad (4)$$

3.1.5. Height (He)

Height (He) is a feature provided by the point cloud at Z-coordinate. Height can be measured from sea level, in case of geo-referenced data, from the lowest point or from the ground (Park and Guldman, 2019; Balado et al., 2018). In either of these situations, in the subsequent normalization phase, the sea level offset is eliminated. Visualising height as a colour gradient allows the verticality and horizontality of environmental elements to be identified, a principle of human psychology to interpret scenes (Selfridge, 1988).

3.1.6. Point density (Pd)

Point density (Pd) is a feature that depends on the laser scanning frequency, the distance between the laser and the target surface and the angle of incidence. It is a relevant feature for highlighting or attenuating isolated points or areas with low point density. Many authors have proposed methods to calculate the point density (Weinmann et al., 2013; Liao et al., 2021; Peng et al., 2021). In this work we use the Eq. (5) for calculate point density based on the distance difference between the first (d_1) and fourth (d_4) closest neighbouring points. This measure was proposed by Pfeifer et al. (2021), however, in order to obtain the delimited values (0–1), the division has been inverted.

$$point_density = \frac{d_1}{d_4} \quad (5)$$

3.1.7. Linearity (Li)

Linearity (Li) is a geometric feature based on the distribution of k neighbouring points from the eigenvalues ($\lambda_1 \lambda_2 \lambda_3$) (Eq. (6)) (Weinmann et al., 2015). Linearity enhances linear elements, e.g. pole like objects (Li et al., 2018), but also corners between two planes. According to many object recognition theories, edges are one of the most important features. According to Marr and Nishihara's theory (Marr et al., 1978), in the first stage of perception, the image is described as edges, spots, bars and the geometrical distribution. According to Biederman's Recognition-by-Components (RBC) theory (Biederman, 1987), geons are simple volumetric shapes and they responsible for object recognition. The first step of recognition would be to extract edges from changes in luminance and, in parallel, the division of the object into concave regions. The RBC/JIM model (Kurbat, 1994; Hummel and Biederman, 1992) consider that recognition occurs in a similar way to neural networks: activation of neurons in successive layers. In the first layer, edges are detected. In layers 2 and 3, geons, symmetry and blobs. In layers 4 and 5, size and orientation of geons. Given the importance of edges, linearity is a very relevant feature for object identification.

$$linearity = \frac{\lambda_1 - \lambda_2}{\lambda_1} \quad (6)$$

3.1.8. Planarity (Pl)

Planarity (Pl) is a geometric feature calculated from the eigenvalues (Eq. (7)) (Weinmann et al., 2015). Planarity enhances flat elements that conform most of the built environment and allow a visualisation of curvature. According to RBC theory, in addition to edge detection, in the construction of 3D representations also are relevant the non-accidental properties (symmetry, parallelism, straightness/curvature and connections), responsible for maintaining the constancy of objects. Therefore, planarity is relevant for identifying geons due to the visualisation of the curvature of the objects.

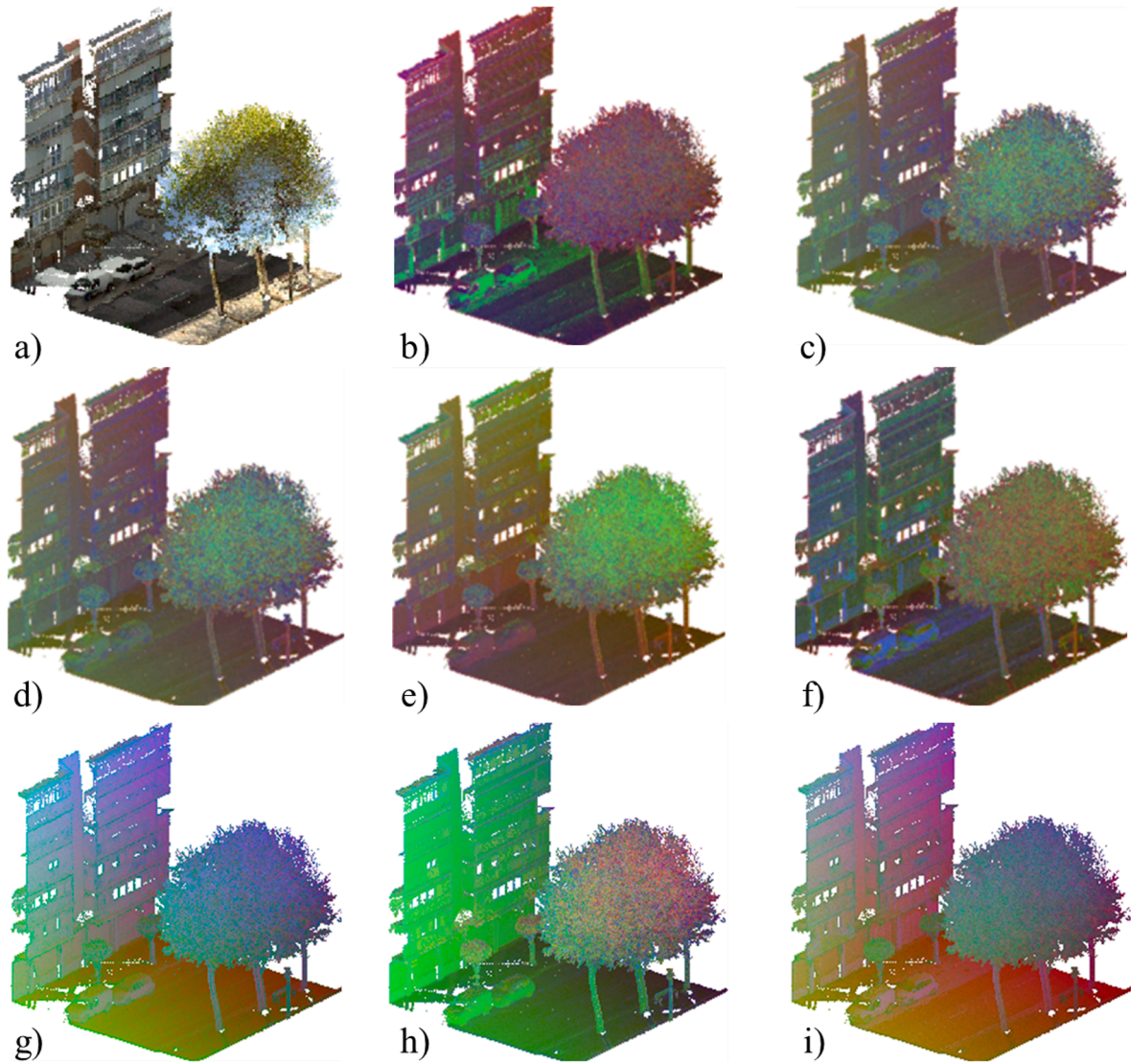


Fig. 3. RGB reference image (a) and the best feature permutation according to MCD (b), MSE (c), PSNR (d), SSIM (e), CSV (f), BRISQUE (g), NIQE (h), and PIQE (i).

$$planarity = \frac{\lambda_2 - \lambda_3}{\lambda_1} \quad (7)$$

3.1.9. Scattering (Sc)

Finally, the scattering (Sc) is a geometric feature calculated from the eigenvalues according to Eq. (8) (Weinmann et al., 2015). Scattering enhances elements of irregular 3D shapes (Munoz et al., 2009). This category includes vegetation (Chen et al., 2021) as well as junctions of three or more planes, so that dispersion is presented as a feature also aligned with edge and geon identification.

$$scattering = \frac{\lambda_3}{\lambda_1} \quad (8)$$

As can be seen from the justification above, there is no one-to-one correspondence between features and perceptual descriptors. Although point cloud features are carefully chosen, many features have interdependencies between them and cover several perceptual descriptors. Also, not all perceptual descriptors have the same relevance for interpreting the scene. Table 1 summarises the relationship between the calculated point cloud features and perceptual descriptors.

3.2. Feature normalization

The selected features have different ranges. The reflectance values depend on the LiDAR tool, so it is difficult to delimit. The return number varies between 1 and 4 usually, although some LiDARs reach 5 returns. The inclination varies between 0° and 90° . Depth and height depend on the volume of the scene. Point density, linearity, planarity, and scattering vary between 0 and 1. Therefore, it is essential to normalize these features to obtain bounded values. Feature normalization is performed between 0 and 1. Reflectance, depth and height are adjusted by Eq. (9). Return number is divided between 4, and inclination angle between 90. Point density, linearity, planarity, and scattering do not require any modification.

$$f_{norm-i} = \frac{f_i - \min(f)}{\max(f) - \min(f)} \quad (9)$$

3.3. Channel permutations and reduction

In order to simultaneously display nine features, it is necessary to combine the features F_n for the final distribution to RGB channels (Fig. 2). The reduction is done through the conversion of 3 features to 1, according to the RGB to greyscale colour conversion (Eq. (10)) with

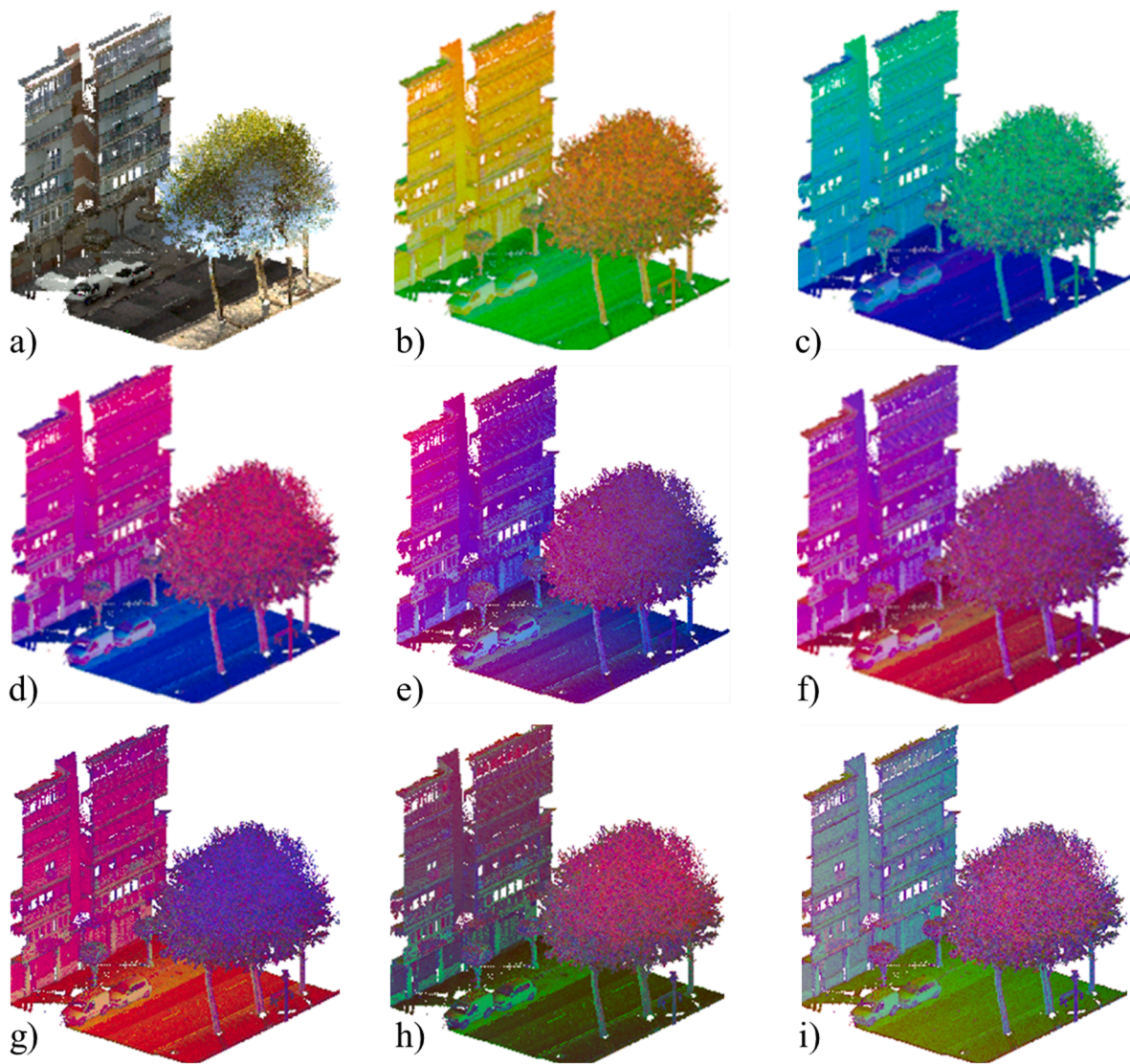


Fig. 4. RGB reference image (a) and the worst feature permutation according to MCD (b), MSE (c), PSNR (d), SSIM (e), CSV (f), BRISQUE (g), NIQE (h), and PIQE (i).

Table 5
Channel permutation sorted by $\sum \text{normalizedQMetrics}$.

Channel permutation (feature order)	$\sum \text{normalizedQMetrics}$
DeLiHeRnReInPlScPd	0.467
HeReInPdLiScDeRnPl	0.468
RnLiDePdReHePlScIn	0.474
HeLiPdRnReInPlScDe	0.474
HeLiInRnRePdDeScPl	0.477
ReHeInPdLiScDeRnPl	0.480
DeLiHeRnReInPdScPl	0.481
ReRnInPdLiScDeHePl	0.482
PdLiInRnReHeDeScPl	0.483
HeLiPlRnReInDeScPd	0.484
...	
RnLiInPlDePdHeScRe	3.133
HeLiRnPlDePdReScIn	3.153
HeLiRePlDePdRnScIn	3.154
HeLiRnPlDePdInScRe	3.192
HeLiInPlDePdRnScRe	3.246

luminance ($E'y$) in Rec.ITU-R BT.601-7 widely used in image processing. A priori, there is no optimal feature order for the combination of the nine features simultaneously, so it is necessary to evaluate all the possibilities. The combination of different elements, without repetition, only

changing order is known as ordered arrangement or permutation ($n!$). Being $n = 9$, the number of possible combinations is 362,880.

$$\text{grey} = 0.299\text{red} + 0.587\text{green} + 0.114\text{blue} \quad (10)$$

3.4. Colour conversion and mean colour distance (MCD) estimation

Once the nine features have been combined into three, associating one to each RGB channel, the input point cloud P with new colour attributes $P(P_x, P_y, P_z, R, G, B)$ can be visualized. This sub-section explains how to evaluate all possible feature permutations and choose the one with the smallest colour deviation with a reference point cloud $P_{REF}(P_{REF_x}, P_{REF_y}, P_{REF_z}, R_{REF}, G_{REF}, B_{REF})$. The CIELAB colour space is more appropriate for calculating colour distances than RGB because distances in CIELAB are consistent with the colour differences perceived by the human eye (Panigrahy et al., 2021). Since many electronic devices capture RGB colour corresponding to standard RGB (sRGB), we will assume conversion from sRGB to CIELAB colour space (Eqs. (11)–(13)) (Bianconi et al., 2009). Also, MLS surveys are conducted in ambient light, typically corresponding to clear days and clear illumination, so the illuminant selected is D65. Illuminant D65 represents average Daylight in Western Europe, with an average colour temperature of 6,504 Kelvin. It is the standard for use in colorimetry ISO

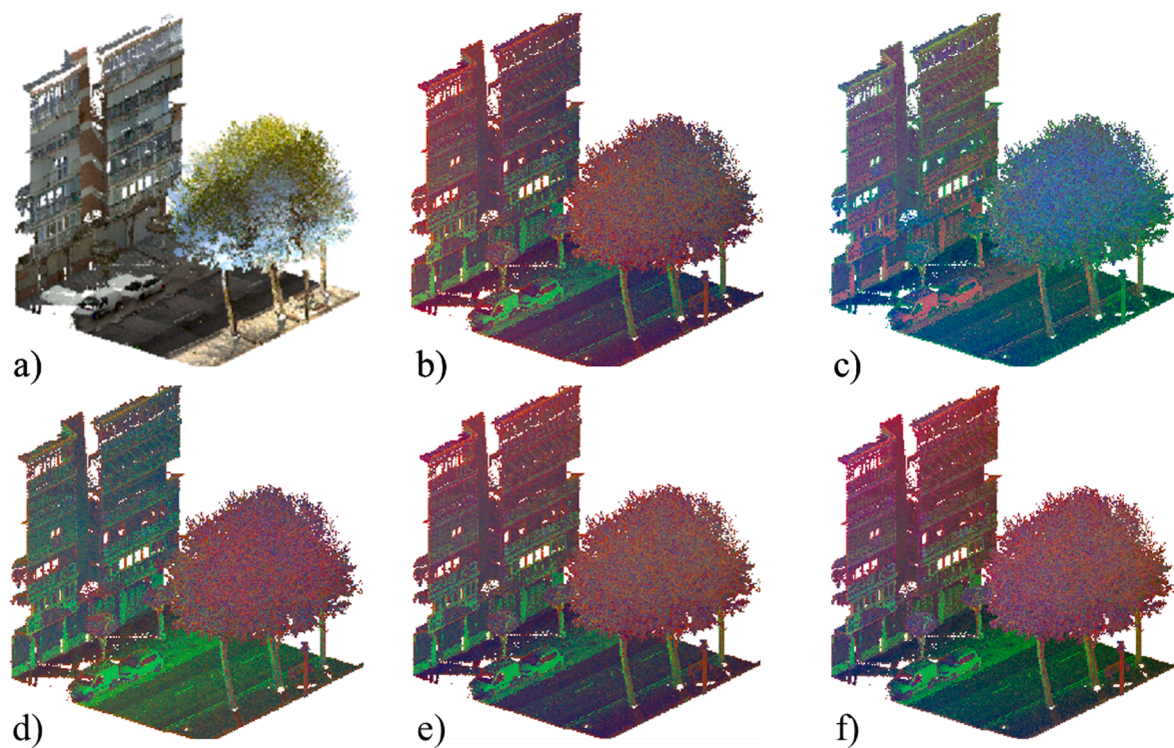


Fig. 5. RGB reference image (a) and the best feature permutation sorted by $\sum \text{normalized QA metrics}$ (b–f).

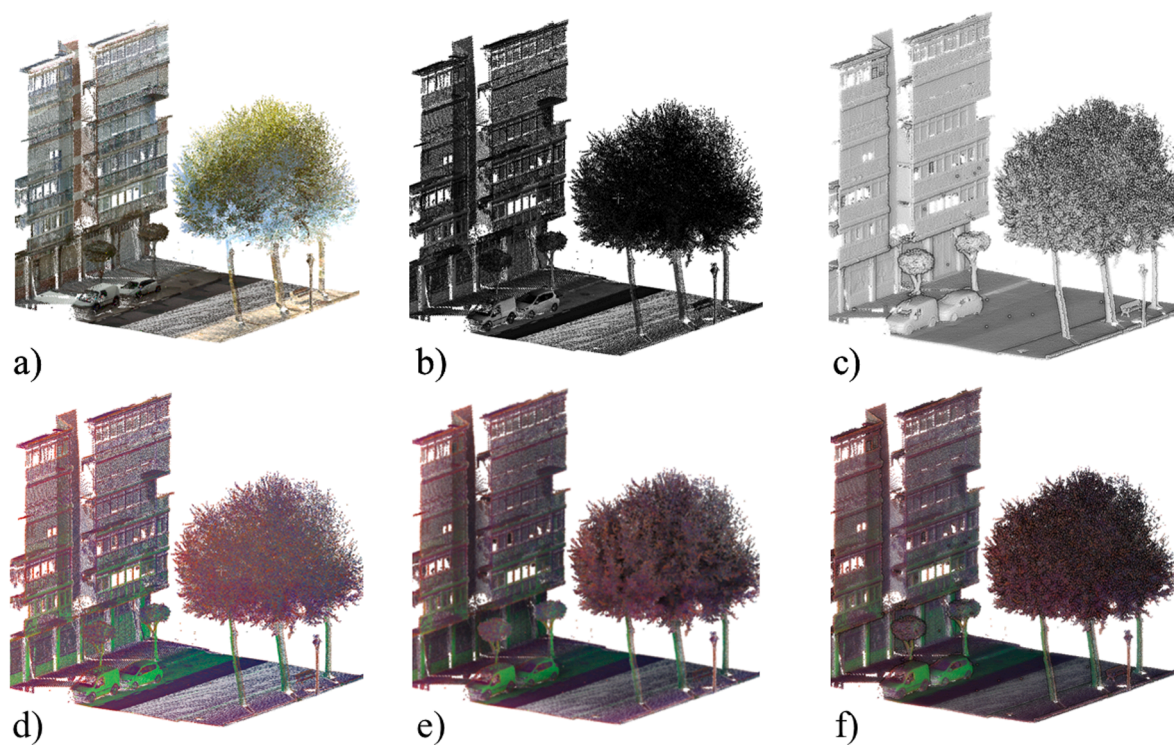


Fig. 6. Comparison between point cloud visualization methods in Cloud Compare: (a) natural RGB, (b) reflectance grayscale, (c) white coloured with EDL, (d) MFRSC, (e) MFRSC with SSAO, and (f) MFRSC with EDL.

Table 6

Values of IQA metric without reference comparing MRSC raster point cloud and natural-coloured raster point cloud.

	BRISQUE	NIQE	PIQE
Best MFRSC feature permutation	34.83	9.276	40.05
Natural-coloured point cloud	44.28	13.53	59.26
Worst MFRSC feature permutation	47.02	15.30	64.61

10526:1999/CIE S 005/F-1998 and CIE S 005/G-1998.

$$\begin{pmatrix} L \\ A \\ B \end{pmatrix} = 100 \begin{bmatrix} 0 & 116 & 0 & -16 \\ 500 & -500 & 0 & 0 \\ 0 & 200 & -200 & 0 \end{bmatrix} \begin{pmatrix} f(X/X_n) \\ f(Y/Y_n) \\ f(Z/Z_n) \\ 1 \end{pmatrix} \quad (11)$$

where and X_n , Y_n and Z_n are the tristimulus values of the illuminant (D65

$$Rot = \begin{bmatrix} \cos\phi*\cos\theta & \cos\phi*\sin\theta*\sin\psi - \cos\phi*\cos\psi & \cos\phi*\sin\theta*\cos\psi - \sin\phi*\sin\psi \\ \sin\phi*\cos\theta & \sin\phi*\sin\theta*\sin\psi - \sin\phi*\cos\psi & \sin\phi*\sin\theta*\cos\psi - \sin\phi*\sin\psi \\ -\sin\theta & \cos\theta*\sin\psi & \cos\theta*\cos\psi \end{bmatrix} \quad (15)$$

in this case):

$$\begin{pmatrix} X_n \\ Y_n \\ Z_n \end{pmatrix} = 100 \begin{bmatrix} 0.4124 & 0.3576 & 0.1805 \\ 0.2126 & 0.7151 & 0.0721 \\ 0.0193 & 0.1192 & 0.9505 \end{bmatrix} \begin{pmatrix} R \\ G \\ B \end{pmatrix} \quad (12)$$

$$f(t) = \begin{cases} t^{1/3} & : 1 \geq t \geq 0.008856 \\ 7.787t + (16/116) & : 0 \leq t \leq 0.008856 \end{cases} \quad (13)$$

The distance estimation between the CIELAB colour values of the input point cloud P and the reference P_{REF} is performed as a distance calculation in three dimensions (Eq. (14)). The mean of the colour deviation of all points is finally calculated.

$$D = \sqrt{(L - L_{REF})^2 + (A - A_{REF})^2 + (B - B_{REF})^2} \quad (14)$$

3.5. Rotation and rasterization

The conversion of the point cloud into an image is necessary to apply the Image Quality Assessment (IQA) metrics. The conversion from point cloud to image is done by the rasterization process on the Z-axis. To obtain a perspective view of the environment, a 3D rotation matrix Rot is applied (Eq. (15)).

being ϕ the rotation angle in axes Z, θ the rotation angle in Y, and ψ the rotation angle in X.

The rasterization process consists of the following steps:

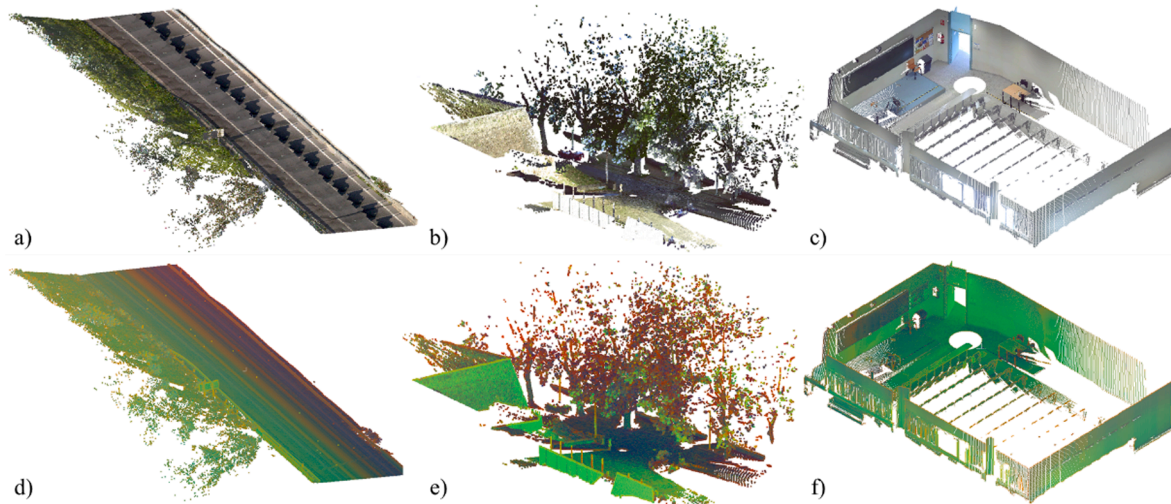


Fig. 7. Comparison between point cloud visualization: MLS highway environment (a) natural-coloured, (d) synthetic-coloured; TLS outdoor (b) natural-coloured, (e) synthetic-coloured; TLS indoor (c) natural-coloured, (f) synthetic-coloured.

Table 7

Processing time for each case study.

Case Study	Number of points	knn calculation (s)	Feature extraction (s)	Feature combination (s)	TOTAL (s)
MLS street	363,820	1.668	109.505	0.004	111.177
MLS highway	447,645	2.031	155.073	0.003	157.107
TLS outdoor	254,798	1.265	64.752	0.004	66.021
TLS indoor	772,890	2.408	221.744	0.005	224.157

Generation of an empty 2D matrix $I(M, N)$ that encompasses the bounding box of the input point cloud in axes XY with a pixel size r . Assignment of the points to matrix cells (pixels) according to the $P_X P_Y$ coordinates.

Assignment of each pixel value according to the feature of the point with the maximum P_Z coordinate.

3.6. Image quality Assessment

Image Quality Assessment (IQA) and PCQA methods can be used not only to evaluate the quality of decoded, rendered, or transmitted PCs, but also to understand the representation and display requirements needed to achieve a good perceived quality of experience for the end-user (Diniz et al., 2021). Seven IQA metrics are implemented to assess the quality of the visualisation of the colour permutations. Four correspond to metrics with reference (the equivalent image of the natural RGB coloured point cloud acquired by the MLS). Three others correspond to metrics without reference. All of them are explained below.

3.6.1. Image quality metrics with reference

- MSE (Sara et al., 2019): Mean Squared Error measures the average squared difference between the actual and reference pixel values. This metric is easy to calculate but may not align well with human perception of quality.
- PSNR (Gupta et al., 2011): Peak Signal-to-Noise Ratio is derived from the MSE, and indicates the ratio of the maximum pixel intensity to the distortion power. It also sometimes fails to give result similar to as perceived by the human visual system.
- SSIM (Wang et al., 2004): Assuming that human visual perception is highly adapted for extracting structural information from scene, the Structural Similarity Index Measure combines local image structure, luminance, and contrast between neighbouring pixels to obtain a more subjective image quality according to human perception.
- CSV (Temel and AlRegib, 2016): Based on Colour, Structure, and Visual system, this estimator quantifies low-level colour degradations, in addition to structural differences (obtained by mean subtraction and divisive normalization) and perceptual feature maps (obtained from contrast sensitivity formulations of retinal ganglion cells).

3.6.2. Image Quality metrics without reference

- BRISQUE (Mittal et al., 2012): Blind/Referenceless Image Spatial Quality Evaluator is trained on a database of images with known distortions, and evaluates the quality of images with the same type of distortion, therefore, the distortion is subjective to the training set.
- NIQE (Mittal et al., 2013): Natural Image Quality Evaluator is based on the construction of a “quality aware” collection of statistical features based on a simple and successful space domain natural scene statistic model. These features are derived from a corpus of natural, undistorted images. The NIQE score of an image may not correlate as well as the BRISQUE score with the human perception of quality.
- PIQE (Chan and Goldsmith, 2000): Psychovisually-based Image Quality Evaluator evaluates the image quality using two psychovisually-based fidelity criteria: blockiness and similarity. PIQE is less computationally efficient than BRISQUE and NIQE, but provides local quality measures in addition to an overall quality score.

4. Experiments

4.1. Case study

The selected case study corresponded to 16 m of the *Avenida de Castilla* in Palencia (Spain). It is a typical urban configuration in the form

of a street with a repetitive pattern. In addition, the case study contains a great variety of urban elements: buildings, parked cars, trees of various species and sizes, road, road markings, sidewalk, streetlamps and furniture. The corresponding point cloud was scanned with Lynx Mobile Mapper (Balado et al., 2017), with a Ladybug5 360° camera. The survey contained 1 million points, but the point density was reduced to accelerate computation. Density reduction was performed by a 3D grid of 5 cm resolution that maintained one point per voxel. The point cloud for tests contained 363 thousand points. For those features that depended on the number of neighbours, $k = 25$ neighbours was set (Weinmann et al., 2015). Subsequently, the feature normalization was applied to dimension values between 0 and 1. The rotation matrix of Equation (16) was used for the perspective view generation. The rasterization used a pixel size $r = 10$ cm, generating images of 260×263 pixels.

$$Rot = \begin{bmatrix} -0.559 & -0.829 & -0.011 \\ 0.325 & -0.231 & 0.917 \\ -0.763 & 0.509 & 0.399 \end{bmatrix} \quad (16)$$

4.2. Results and analysis

Tables 2–4 show the permutations of features ordered according to the values of each metric. Also, Fig. 3 compiles the best feature permutation for each metric while Fig. 4 compiles the worst permutation. Overall, the analysis of the QA metrics without a visual support is quite confusing due to the difference in range values between the metrics and abstraction of results. Therefore, a joint view of Tables 2–4 and Figs. 3 and 4 is recommended, which directly allows relating the quantification of the metrics to the subjective human visual perception provided by the images.

The first remarkable issue is the large colour distance between the natural RGB colour and any permutation. In the best case, the Mean Colour Distance (MCD) obtained is 44.47 colour units (Fig. 3.b), a similar value to the distance from orange to red. It is therefore not possible to obtain a synthetic colour close to the natural colour with only multiple features. However, the best feature order permutation according to MCD allows a clear view of the scene and the direct identification of vehicles, parking areas, road markings, trees, and buildings.

The valuations of the IQA metrics are not always related to subjective human visual perception. This was indicated by other authors (Torlig et al., 2018; Cruz et al., 2019; Alexiou et al., 2018) and it was also observed in the present results. In tests performed with IQA metrics with reference it is difficult to assess whether the quality of the visualization corresponds to the metric and thus, to a particular order of features. Comparing the best and worst feature permutation presented in Fig. 3.c-f and Fig. 4.c-f, there is no clear distinction which feature order provides better visualization; except for MSE, for which the worst feature permutation only highlights inclination (Fig. 4.c). In all other metrics (PSNR, SSIM, and CSV), the best and worst feature permutation offer similar visual perceptions beyond the change in colour palette.

As for the IQA metrics without reference (BRISQUE, NIQE, PIQE), the expected result was completely opposite. Since these metrics greatly penalize distortions, in the case of point cloud raster, the IQA metrics without reference considered distortions every detail that provide information to the scene. E.g., in the best feature permutation according to BRISQUE (Fig. 3.g) and PIQE (Fig. 3.i), it is very difficult to distinguish even the cars, which were clearly identifiable with IQA metrics with reference. In contrast, the worst feature permutation (Fig. 4.g–i) provides images where many details and objects are clearly distinguishable.

In order to obtain a joint view of all permutations providing a better visualization according to all QA metrics, the values of several metrics were combined. For this purpose, given the large variation (range of values) between QA metrics, the values were normalized between 0 and 1 taking as reference the minimum and maximum value of each metric (Eq. (9)). The IQA metrics with reference were discarded from this

overall assessment, since in this case, IQA metrics are not related to human visual perception, as discussed above. The IQA metrics without reference were reversed, since higher values indicate worse visualizations but correspond to more rich subjective visualization, as discussed above. Therefore, the QA used in the joint assessment were the MCD, BRISQUE, NIQE and PIQE. The results obtained are shown in Table 5 and Fig. 5.

As can be seen in Fig. 5, the five best feature permutation according to \sum normalized QA metrics offer a good subjective visualization and identification of objects in urban scene. The order of features in the best permutations was similar and, consequently, the synthetic colours produced were also similar (except for Fig. 5.c). A clear similarity can be observed between the first and fourth position (Fig. 5.b and .e), where the road had a dark colour closer to the asphalt and that provides a greater contrast between asphalt and other objects, but not with the sidewalk. Another clear similarity can be observed with the third and fifth position (Fig. 5.d and .f), only practically changing the tonality of the road. MFRSC allows to recognize objects and to distinguish their component parts, since each part usually has a specific geometry and reflectance, and in many cases associated with different natural colours. Thus, in the synthetically coloured images in Fig. 5, it is possible to distinguish windows and doors of buildings, trunks and foliage of trees, and windshields and wheels of cars easily.

ademas de reconocer objetos, las partes que pudiendo asi no solo reconocer objetos sino Tambien las partes que los component.

5. Discussion

The proposed Multi Feature-Rich Synthetic Colour (MFRSC) provides a correct visualization of the urban environment. It is obvious that the synthetic colour obtained is far from the natural colour, so it is not possible to obtain a realistic environment. However, the MFRSC perfectly replaces the natural colour and different objects can be identified correctly in the synthetic-coloured environment. Moreover, the MFRSC implies other advantage: the visualization is not subject to colouring errors. Colour projection from cameras on the point cloud may be erroneous due to the inadequate calibration of the photographic equipment or to the geometry, visibility, and occlusions of the 3D environment. It is therefore a good alternative for viewing coloured point clouds if natural colour information is not available.

The selection of the optimal feature permutation considered the Mean Colour Distance (MCD) between natural and synthetic colour, since a relation between MCD results and visual perception was shown. The authors consider that the use of close-to-natural colours improves the human perception. Colour is a feature highly dependent on the environment. Colour of cars or buildings can change; however, many urban elements have a colour that can be assumed to be constant (e.g., green for trees, black for asphalt, or white for road markings), so having a colour reference is important for the selection of the optimal feature permutation.

MFRSC focuses on natural colour substitution, so synthetic colour generation allows the display of coloured point clouds even in the vast amount of software that does not support colourization based on point attributes (Otepka et al., 2020). In addition, MFRSC allows a more complete visualization of point clouds simultaneously displaying nine features than single point attribute visualization. Other advantages are the possible combination of MFRSC with other non-photorealistic techniques based on illumination and occluders such as EDL or Screen Space Ambient Occlusion (SSAO) (Fig. 6). Illumination-based techniques calculate shadows from depth buffers in the 3D geometry and generate a shadow image that is combined with the colour rendering of the scene (in this case, the synthetic colour generated with MFRSC).

The application of BRISQUE, NIQE and PIQE metrics to the raster images of the natural-coloured point cloud indicated values in the middle of feature permutations of MFRSC (Table 6). This indicates that a significant number of feature permutations offer a lower distortion

visualization than the natural-coloured point cloud. However, the interpretation of these metrics does not have a clear and direct correlation with human perception either.

The best MFRSC feature permutation was also applied to other three case studies, not involved in the test already performed for the QA. Natural and synthetic colour are shown in Fig. 7. The new point clouds corresponded to:

- Highway environment scanned with Lynx Mobile Mapper.
- Outdoor environment scanned with Terrestrial Laser Scanning (TLS) Faro Focus X330.
- Indoor environment scanned with TLS Faro Focus X330.

The results of the application to the other case studies followed a similar behaviour to that already tested. The visualization of some elements was improved, such as the lower guardrail in the highway. Some shades similar to the natural colour were maintained, such as the slate in the classroom. A sense of depth was also maintained in all the case studies and edges were highlighted. However, some elements had not as much contrast compared to the natural colour, such as the differentiation of the slope with vegetation and the road.

The method was implemented in Matlab® 2021a, on a computer i7-7700HQ CPU 2.80 GHz 16 GB RAM. The processing times for all case studies are listed in Table 7. The processing time depends on the number of points. The case study that took the longest time was the TLS indoor point cloud with almost four minutes, as it was the largest with 772,890 points. The 98% of the time was consumed by the feature extraction process. Although the programming language used is primarily for prototyping, and the translation to other languages will improve the computation time, feature extraction is not considered real time today, so the method have to be executed offline, already done in other visualization works, e.g. continuous LoD (van Oosterom et al., 2022). On the other hand, feature combination is a millisecond process, but the analysis of all QA for all permutations of the test case study took 24 h. This process is extremely slow and, although it provides the optimal visualization for each case study, it can be substituted by the use of the feature order recommended in this work which has shown satisfactory visualizations in other case studies.

6. Conclusion

This work presents a Multi Feature-Rich Synthetic Colour (MFRSC) approach to replace the natural colour of point clouds. Nine features were selected according to five visual perception descriptors related to human visual perception and distributed over the three RGB channels (after 9 to 3 reduction process). The nine features were reflectance, return number, inclination, depth, height, point density, linearity, planarity, and scattering. The five visual perception descriptors were edges, texture, shape, size, depth, orientation. The method was tested on an MLS point cloud of real 3D urban environment. All possible feature permutations were analysed according to colour distance and IQA metrics with and without reference, selecting those that offered the best final visualization. As a result, it was observed that, by the mean of colour distance and BRISQUE, NIQE and PIQE metrics, it was possible to uniform the values and obtain those features permutations with a better subjective visualization.

As a conclusion, the MFRSC allows an alternative colouring to the natural colour for point clouds. MFRSC can provide a framework composed by feature extraction, normalization, and channel reduction in which the optimal visualization can be estimated by brute force search. Since the force search requires a long computation time, the test MLS urban point cloud provided the optimal feature permutation (Depth-Linear-Height for channel R, Return-Reflectance-Inclination for channel G, and Planar-Scatter-Density for channel B) that offers a correct distinction of all objects in the urban scene. In addition, this permutation of channels and features shown good results in MLS point

clouds for road environments and TLS point clouds for outdoor and indoor environments. The method can be implemented for simultaneous visualization of multiple features in software that does not support colourization based on point attributes and combined with other non-photorealistic techniques such as EDL and AO.

The features used are easily and quickly computable, and they are available in almost all laser scanning devices, so technically MFRSC can be applied to all types of scenes and laser scanners. However, since point clouds acquired by different platforms have different geometric and radiometric specifications, also related to the 3D scene and perspective, perception of MFRSC may be affected. The future work will evaluate the application of MFRSC to Handled and Aerial Laser Scanning in other relevant environments, such as country areas or cultural heritage sites. Future work will also focus on study if MRSC is a suitable solution for immersive point cloud visualization in Virtual Reality devices. Finally, Deep Learning techniques will be applied to semantically segment the point cloud and relate the parts of each object to a synthetic colour or generate natural colour directly from Generative Adversarial Networks.

Declaration of Competing Interest

The authors declare that they have no known competing financial interests or personal relationships that could have appeared to influence the work reported in this paper.

Acknowledgements

This research has received funding from Xunta de Galicia through human resources grant (ED481B-2019-061), GAIN (grant number ED431F 2022/08) and from the Government of Spain through project PID2019-105221RB-C43 funded by MCIN/AEI/10.13039/501100011033. This paper was carried out in the framework of the InfraROB project (Maintaining integrity, performance and safety of the road infrastructure through autonomous robotized solutions and modularization), which has received funding from the European Union's Horizon 2020 research and innovation programme under grant agreement no. 955337. It reflects only the authors' views. Neither the European Climate, Infrastructure, and Environment Executive Agency (CINEA) nor the European Commission is in any way responsible for any use that may be made of the information it contains. Funding for open access charge: Universidade de Vigo/CISUG.

References

- 3D Object Recognition System Based On Local Shape Descriptors and Depth Data Analysis, Recent Patents Comput. Sci., 2019.12.
- Abdelhafiz, A., 2013. Laser scanner point cloud colouring algorithm applied on real site. *Surv. Rev.* 45, 343–351. <https://doi.org/10.1179/1752270612Y.0000000031>.
- Alexiou, E., Ebrahimi, T., 2017. On the performance of metrics to predict quality in point cloud representations. In: *Proc. SPIE*. doi:10.1117/12.2275142.
- Alexiou, E., Ebrahimi, T., 2019. Exploiting user interactivity in quality assessment of point cloud imaging. In: 2019 IEEE Int. Conf. Qual. Multimed. Exp. pp. 1–6. doi: 10.1109/QoMEX.2019.8743277.
- Alexiou, E., Ebrahimi, T., Bernardo, M.V., Pereira, M., Pinheiro, A., Cruz, L.A.D.S., Duarte, C., Dmitrovic, L.G., Dumic, E., Matkovics, D., Skodras, A., 2018. Point cloud subjective evaluation methodology based on 2D rendering. In: 2018 Tenth Int. Conf. Qual. Multimed. Exp., pp. 1–6. <https://doi.org/10.1109/QoMEX.2018.8463406>.
- Alexiou, E., Xu, P., Ebrahimi, T., 2019. Towards modelling of visual saliency in point clouds for immersive applications. In: 2019 IEEE Int. Conf. Image Process., pp. 4325–4329. <https://doi.org/10.1109/ICIP.2019.8803479>.
- Ali, M.E.N.O., Taha, L.-G.-E.-D., Mohamed, M.H.A., Mandouh, A.A., 2021. Generation of digital terrain model from multispectral LiDAR using different ground filtering techniques. *Egypt. J. Remote Sens. Sp. Sci.* 24, 181–189. <https://doi.org/10.1016/j.ejrs.2020.12.004>.
- Aliev, K.-A., Sevastopolsky, A., Kolos, M., Ulyanov, D., Lempitsky, V., 2020. Neural point-based graphics. In: Vedaldi, A., Bischof, H., Brox, T., Frahm, J.-M. (Eds.), *Comput. Vis. – ECCV 2020*, Springer International Publishing, Cham, pp. 696–712.
- Balado, J., Díaz-Vilariño, L., Arias, P., Soilán, M., 2017. Automatic building accessibility diagnosis from point clouds. *Autom. Constr.* 82, 103–111. <https://doi.org/10.1016/j.autcon.2017.06.026>.
- Balado, J., Díaz-Vilariño, L., Arias, P., González-Jorge, H., 2018. Automatic classification of urban ground elements from mobile laser scanning data. *Autom. Constr.* 86, 226–239. <https://doi.org/10.1016/j.autcon.2017.09.004>.
- Bavoil, L., Sainz, M., 2009. Multi-layer dual-resolution screen-space ambient occlusion. In: *SIGGRAPH 2009 Talks*, Association for Computing Machinery, New York, NY, USA. doi:10.1145/1597990.1598035.
- Bianconi, F., Fernández, A., González, E., Caride, D., Calviño, A., 2009. Rotation-invariant colour texture classification through multilayer CCR. *Pattern Recognit. Lett.* 30, 765–773. <https://doi.org/10.1016/j.patrec.2009.02.006>.
- Biederman, I., 1987. Recognition-by-components: a theory of human image understanding. *Psychol. Rev.* 94, 115.
- Boucheny, C., Ribes, A., 2011. Eye-dome lighting: a non-photorealistic shading technique. *Kitware Source Q. Mag.* 17.
- Burwell, C., Jarvis, C., Tansey, K., 2012. The potential for using 3D visualization for data exploration, error correction and analysis of LiDAR point clouds. *Rem. Sens. Lett.* 3, 481–490. <https://doi.org/10.1080/01431161.2011.629233>.
- Chan, R.W., Goldsmith, P.B., 2000. A psychovisually-based image quality evaluator for JPEG images. In: *Smc 2000 Conf. Proceedings. 2000 IEEE Int. Conf. Syst. Man Cybern. 'cybernetics Evol. to Syst. Humans, Organ. Their Complex Interact. Cat. No.0, 2000*: pp. 1541–1546 vol. 2. doi:10.1109/ICSMC.2000.886075.
- Chen, Y., Wu, R., Yang, C., Lin, Y., 2021. Urban vegetation segmentation using terrestrial LiDAR point clouds based on point non-local means network. *Int. J. Appl. Earth Obs. Geoinf.* 105, 102580 <https://doi.org/10.1016/j.jag.2021.102580>.
- Chiu, Y.-P., Lo, S.-K., Hsieh, A.-Y., 2017. How colour similarity can make banner advertising effective: insights from Gestalt theory. *Behav. Inf. Technol.* 36, 606–619. <https://doi.org/10.1080/0144929X.2016.1267264>.
- Colomb, M., Duthon, P., Bernardin, F., 2019. Spectral reflectance characterization of the road environment to optimize the choice of autonomous vehicle sensors*. In: 2019 IEEE Intell. Transp. Syst. Conf., 2019, pp. 1085–1090. doi:10.1109/ITSC.2019.8917455.
- Cruz, L.A. da S., Dumić, E., Alexiou, E., Prazeres, J., Duarte, R., Pereira, M., Pinheiro, A., Ebrahimi, T., 2019. Point cloud quality evaluation: towards a definition for test conditions. In: 2019 Elev. Int. Conf. Qual. Multimed. Exp., 2019, pp. 1–6. doi: 10.1109/QoMEX.2019.8743258.
- Deibe, D., Amor, M., Doallo, R., 2019. Supporting multi-resolution out-of-core rendering of massive LiDAR point clouds through non-redundant data structures. *Int. J. Geogr. Inf. Sci.* 33, 593–617. <https://doi.org/10.1080/13658816.2018.1549734>.
- Diniz, R., Freitas, P.G., Farias, M.C.Q., 2020. Multi-distance point cloud quality assessment. In: 2020 IEEE Int. Conf. Image Process., pp. 3443–3447. doi:10.1109/ICIP40778.2020.9190956.
- Diniz, R., Freitas, P.G., Farias, M.C.Q., 2020. Towards a point cloud quality assessment model using local binary patterns. In: 2020 Twelfth Int. Conf. Qual. Multimed. Exp., pp. 1–6. doi:10.1109/QoMEX48832.2020.9123076.
- Diniz, R., Freitas, P.G., Farias, M., 2021. A novel point cloud quality assessment metric based on perceptual color distance patterns. *Electron. Imaging*. 2021, 251–256.
- Discher, S., Richter, R., Döllner, J., A scalable WebGL-based approach for visualizing massive 3D point clouds using semantics-dependent rendering techniques. In: *Proc. 23rd Int. ACM Conf. 3D Web Technol.*, Association for Computing Machinery, New York, NY, USA. doi:10.1145/3208806.3208816.
- Discher, S., Masopust, L., Schulz, S., Richter, R., Döllner, J., 2018. A point-based and image-based multi-pass rendering technique for visualizing massive 3D point clouds in VR environments. *J. WSCG*. 26, doi:10.24132/JWSCG.2018.26.2.2.
- Discher, S., Richter, R., Döllner, J., 2019. Concepts and techniques for web-based visualization and processing of massive 3D point clouds with semantics. *Graph. Models*. 104, 101036 <https://doi.org/10.1016/j.gmod.2019.101036>.
- Edler, D., Keil, J., Dickmann, F., 2020. From Na Pali to Earth—An 'Unreal' Engine for Modern Geodata? BT - modern approaches to the visualization of landscapes. In: Edler, D., Jenal, C., Kühne, O. (Eds.), *Springer Fachmedien Wiesbaden*, Wiesbaden. pp. 279–291. doi:10.1007/978-3-658-30956-5_15.
- Ekhtari, N., Glennie, C., Fernandez-Diaz, J.C., 2018. Classification of airborne multispectral lidar point clouds for land cover mapping. *IEEE J. Sel. Top. Appl. Earth Obs. Remote Sens.* 11, 2068–2078. <https://doi.org/10.1109/JSTARS.2018.2835483>.
- Estes, J.E., Hajic, E.J., Tinney, L., 1983. Fundamentals of image analysis: analysis of visible and thermal infrared data. In: *Man. Remote Sens. 1*, American Society of Photogrammetry, pp. 987–1124.
- Golovinskiy, A., Kim, V.G., Funkhouser, T., 2009. Shape-based recognition of 3d point clouds in urban environments. In: *IEEE 12th Int. Conf. Comput. Visi.*, pp. 2154–2161. <https://doi.org/10.1109/ICCV.2009.5459471>.
- González, E., Balado, J., Arias, P., Lorenzo, H., 2022. Realistic correction of sky-coloured points in Mobile Laser Scanning point clouds. *Opt. Laser Technol.* 149, 107807 <https://doi.org/10.1016/j.optlastec.2021.107807>.
- Guan, H., Yan, W., Yu, Y., Zhong, L., Li, D., 2018. Robust traffic-sign detection and classification using mobile LiDAR data with digital images. *IEEE J. Sel. Top. Appl. Earth Obs. Remote Sens.* 11, 1715–1724. <https://doi.org/10.1109/JSTARS.2018.2810143>.
- Gupta, P., Srivastava, P., Bhardwaj, S., Bhateja, V., 2011. A modified PSNR metric based on HVS for quality assessment of color images. In: 2011 Int. Conf. Commun. Ind. Appl., pp. 1–4. doi:10.1109/ICCIIndA.2011.6146669.
- Hieu, N.M., Sanghyun, Y., Sungha, J., Sangyoon, P., Joon, H., 2022. B-EagleV: visualization of big point cloud datasets in civil engineering using a distributed computing solution. *J. Comput. Civ. Eng.* 36, 4022005. [https://doi.org/10.1061/\(ASCE\)CP.1943-5487.0001021](https://doi.org/10.1061/(ASCE)CP.1943-5487.0001021).
- Hofer, H., Seitner, F., Gelautz, M., 2018. An end-to-end system for real-time dynamic point cloud visualization. In: 2018 Int. Conf. 3D Immers., pp. 1–8. doi:10.1109/IC3D.2018.8657915.

- Höfle, B., Pfeifer, N., 2007. Correction of laser scanning intensity data: data and model-driven approaches. *ISPRS J. Photogramm. Remote Sens.* 62, 415–433. <https://doi.org/10.1016/j.isprsjprs.2007.05.008>.
- Hummel, J.E., Biederman, I., 1992. Dynamic binding in a neural network for shape recognition. *Psychol. Rev.* 99, 480–517. <https://doi.org/10.1037/0033-295X.99.3.480>.
- Javaheri, A., Brites, C., Pereira, F., Ascenso, J., 2017. Subjective and objective quality evaluation of 3D point cloud denoising algorithms. In: 2017 IEEE Int. Conf. Multimed. Expo Work., pp. 1–6. <https://doi.org/10.1109/ICMEW.2017.8026263>.
- Kurbat, M.A., 1994. Structural description theories: Is RBC/JIM a general-purpose theory of human entry-level object recognition? *Perception* 23, 1339–1368. <https://doi.org/10.1068/p231339>.
- Li, Q., Cheng, X., 2018. Comparison of different feature sets for TLS point cloud classification. *Sensors* 18 <https://doi.org/10.3390/s18124206>.
- Li, L., Hasegawa, K., Nii, I., Tanaka, S., 2019. Fused transparent visualization of point cloud data and background photographic image for tangible cultural heritage assets. *ISPRS Int. J. Geo-Information* 8 <https://doi.org/10.3390/ijgi8080343>.
- Li, F., Lehtomäki, M., Oude Elberink, S., Vosselman, G., Puttonen, E., Kukko, A., Hyypä, J., 2018. Pole-like road furniture detection in sparse and unevenly distributed Mobile Laser Scanning data. *ISPRS Ann. Photogramm. Remote Sens. Spat. Inf. Sci.* IV–2, 185–192. <https://doi.org/10.5194/isprs-annals-IV-2-185-2018>.
- Liao, R., Yang, L., Ma, L., Yang, J., Zhu, J., 2021. A dense 3-D point cloud measurement based on 1-D background-normalized Fourier transform. *IEEE Trans. Instrum. Meas.* 70, 1–12. <https://doi.org/10.1109/TIM.2021.3075740>.
- Liu, Z., Fu, R., Wang, L., Jin, Y., Papakostas, T., Mainelli, X.U., Voûte, R., Verbree, E., BV, C.G.I.N., 2021. Game engine-based point cloud visualization and perception for situation awareness of crisis indoor environments. In: 16th Int. Conf. Locat. Based Serv., p. 183.
- Liu, H., Oosterom, P., Meijers, M., Guan, X., Verbree, E., Horhammer, M., 2020. HISTSFC: optimization for ND massive spatial points querying. *Int. J. Database Manag. Syst.* 12, 7–28. <https://doi.org/10.5121/ijdm.2020.12302>.
- Ma, L., Li, Y., Li, J., Wang, C., Wang, R., Chapman, A.M., 2018. Mobile laser scanned point-clouds for road object detection and extraction: a review. *Remote Sens.* 10 <https://doi.org/10.3390/rs10101531>.
- Ma, L., Li, Y., Li, J., Zhong, Z., Chapman, M.A., 2019. Generation of horizontally curved driving lines in hd maps using mobile laser scanning point clouds. *IEEE J. Sel. Top. Appl. Earth Obs. Remote Sens.* 12, 1572–1586. <https://doi.org/10.1109/JSTARS.2019.2904514>.
- Marr, D., Nishihara, H.K., Brenner, S., 1978. Representation and recognition of the spatial organization of three-dimensional shapes. *Proc. R. Soc. London. Ser. B. Biol. Sci.* 200, 269–294. <https://doi.org/10.1098/rspb.1978.0020>.
- Martinez Rubi, O., Verhoeven, S., van Meersbergen, M., Schütz, M., Oosterom, P., Gonçalves, R., Tijssen, T., 2015. Taming the beast: free and open-source massive point cloud web visualization. doi:10.13140/RG.2.1.1731.4326/1.
- Meynet, G., Digne, J., Lavoué, G., 2019. PC-MSDM: a quality metric for 3D point clouds. In: 2019 Elev. Int. Conf. Qual. Multimed. Exp. pp. 1–3. doi:10.1109/QoMEX.2019.8743313.
- Mittal, A., Moorthy, A.K., Bovik, A.C., 2012. No-reference image quality assessment in the spatial domain. *IEEE Trans. Image Process.* 21, 4695–4708. <https://doi.org/10.1109/TIP.2012.2214050>.
- Mittal, A., Soundarajan, R., Bovik, A.C., 2013. Making a “Completely Blind” image quality analyzer. *IEEE Signal Process. Lett.* 20, 209–212. <https://doi.org/10.1109/LSP.2012.2227726>.
- Mouriño, S. d. P., Balado, J., Arias, P., 2021. Multiview rasterization of street cross-sections acquired with mobile laser scanning for semantic segmentation with convolutional neural networks. In: IEEE EUROCON 2021 – 19th Int. Conf. Smart Technol., pp. 35–39. doi:10.1109/EUROCON52738.2021.9535645.
- Munoz, D., Vandapel, N., Hebert, M., 2009. Onboard contextual classification of 3-D point clouds with learned high-order Markov Random Fields. In: 2009 IEEE Int. Conf. Robot. Autom., pp. 2009–2016. <https://doi.org/10.1109/ROBOT.2009.5152856>.
- Nelson, M., Radhakrishnan, S., Chatterjee, A., Sekharan, C.N., 2015. On compressing massive streaming graphs with Quadrees. In: 2015 IEEE Int. Conf. Big Data (Big Data), pp. 2409–2417. <https://doi.org/10.1109/BigData.2015.7364035>.
- Nik Effendi, N.A.F., Mohd Zaki, N.A., Abd Latif, Z., Suratman, M.N., Bohari, S.N., Zainal, M.Z., Omar, H., 2021. Unlocking the potential of hyperspectral and LiDAR for above-ground biomass (AGB) and tree species classification in tropical forests. *Geocarto Int.* 1–26. <https://doi.org/10.1080/10106049.2021.1990419>.
- O'Connor, Z., 2015. Colour, contrast and gestalt theories of perception: the impact in contemporary visual communications design. *Color Res. Appl.* 40, 85–92. <https://doi.org/10.1002/col.21858>.
- Oliva, S.T., Pérez-Sust, P., 2008. Sistema visual: la percepción del mundo que nos rodea. *Offarm Farm. y Soc.* 27, 98–102.
- Otepka, J., Mandlbürger, G., Schütz, M., Pfeifer, N., Wimmer, M., 2020. Efficient loading and visualization of massive feature-rich point clouds without hierarchical acceleration structures. *Int. Arch. Photogramm. Remote Sens. Spat. Inf. Sci.* XLIII-B2-2, 293–300. <https://doi.org/10.5194/isprs-archives-XLIII-B2-2020-293-2020>.
- Özdemir, E., Remondino, F., Golkar, A., 2019. Aerial point cloud classification with Deep Learning and Machine Learning algorithms. *Int. Arch. Photogramm. Remote Sens. Spat. Inf. Sci.* XLII-4/W18, 843–849. <https://doi.org/10.5194/isprs-archives-XLII-4-W18-843-2019>.
- Panigrahy, C., Seal, A., Mahato, N.K., 2021. A new technique for estimating fractal dimension of color images BT: In: Bhattacharjee, D., Kole, D.K., Dey, N., Basu, S., Plewczynski, D. (Eds.), *Proc. Int. Conf. Front. Comput. Syst.* Springer, Singapore, pp. 257–265.
- Park, Y., Guldman, J.-M., 2019. Creating 3D city models with building footprints and LIDAR point cloud classification: a machine learning approach. *Comput. Environ. Urban Syst.* 75, 76–89. <https://doi.org/10.1016/j.compenvurbysys.2019.01.004>.
- Peng, X., Zhao, A., Chen, Y., Chen, Q., Liu, H., 2021. Tree height measurements in degraded tropical forests based on UAV-LiDAR data of different point cloud densities: a case study on *Dacrydium pierrei* in China. *For.* 12 <https://doi.org/10.3390/f12030328>.
- Pfeifer, N., Falkner, J., Bayr, A., Eysn, L., Ressel, C., 2021. Test charts for evaluating imaging and point cloud quality of mobile mapping systems for urban street space acquisition. *Rem. Sens.* 13 <https://doi.org/10.3390/rs13020237>.
- Placitelli, A.P., Gallo, L., 2011. Low-cost augmented reality systems via 3D point cloud sensors. In: 2011 Seventh Int. Conf. Signal Image Technol. Internet-Based Syst., pp. 188–192. <https://doi.org/10.1109/SITIS.2011.43>.
- Quinlan, P.T., Wilton, R.N., 1998. Grouping by proximity or similarity? Competition between the gestalt principles in vision. *Perception* 27, 417–430. <https://doi.org/10.1068/p270417>.
- Remondino, F., 2003. From point cloud to surface: the modeling and visualization problem. *Int. Arch. Photogramm. Remote Sens. Spat. Inf. Sci.* 34.
- Ren, L., Song, Y., 2022. AOGAN: A generative adversarial network for screen space ambient occlusion. *Comput. Vis. Media* 8, 483–494. <https://doi.org/10.1007/s41095-021-0248-2>.
- Richter, R., Döllner, J., 2010. Out-of-core real-time visualization of massive 3D point clouds. In: Proc. 7th Int. Conf. Comput. Graph. Virtual Reality, Vis. Interact. Africa, Association for Computing Machinery, New York, NY, USA, pp. 121–128. doi: 10.1145/1811158.1811178.
- Richter, R., Döllner, J., 2014. Concepts and techniques for integration, analysis and visualization of massive 3D point clouds. *Comput. Environ. Urban Syst.* 45, 114–124. <https://doi.org/10.1016/j.compenvurbysys.2013.07.004>.
- Sara, U., Akter, M., Uddin, M.S., 2019. Image quality assessment through FSIM, SSIM, MSE and PSNR—a comparative study. *J. Comput. Commun.* 7, 8–18.
- Schütz, M., Ohrhallinger, S., Wimmer, M., 2020. Fast out-of-core octree generation for massive point clouds. *Comput. Graph. Forum* 39, 155–167. <https://doi.org/10.1111/cgf.14134>.
- Schütz, M., Mandlbürger, G., Otepka, J., Wimmer, M., 2020. Progressive real-time rendering of one billion points without hierarchical acceleration structures. *Comput. Graph. Forum* 39, 51–64. <https://doi.org/10.1111/cgf.13911>.
- Schwarz, S., Preda, M., Baroncini, V., Budagavi, M., Cesar, P., Chou, P.A., Cohen, R.A., Krivokuća, M., Lasserre, S., Li, Z., Llach, J., Mammou, K., Mekuria, R., Nakagami, O., Siahaan, E., Tabatabai, A., Tourapis, A.M., Zakharchenko, V., 2019. Emerging MPEG standards for point cloud compression. *IEEE J. Emerg. Sel. Top. Circuits Syst.* 9, 133–148. <https://doi.org/10.1109/JETCAS.2018.2885981>.
- Selfridge, O.G., 1988. Pandemonium: a paradigm for learning. In: *Neurocomputing Found. Res.*, MIT Press, Cambridge, MA, USA, pp. 115–122.
- Shi, P., Billeter, M., Eisemann, E., 2022. Stereo-consistent screen-space ambient occlusion. *Proc. ACM Comput. Graph. Interact. Tech.* 5 <https://doi.org/10.1145/3522614>.
- Soilán, M., Riveiro, B., Balado, J., Arias, P., 2020. Comparison of heuristic and deep learning-based methods for ground classification from aerial point clouds. *Int. J. Digit. Earth* 13 <https://doi.org/10.1080/17538947.2019.1663948>.
- Spehr, N.A.M., Schilling, A., Gumhold, S., Maas, H.-G., 2010. Automatic feature matching between digital images and 2D representations of a 3D laser scanner point cloud. *Int. Arch. Photogramm. Remote Sens. Spat. Inf. Sci.* 38-5, 446–451.
- Temel, D., AlRegib, G., 2016. CSV: Image quality assessment based on color, structure, and visual system. *Signal Process. Image Commun.* 48, 92–103. <https://doi.org/10.1016/j.image.2016.08.008>.
- Tham, J.S., Chang, Y.C., Fauzi, M.F.A., Gwak, J., 2015. Object recognition using depth information of a consumer depth camera. In: 2015 Int. Conf. Control. Autom. Inf. Sci., pp. 203–208. doi:10.1109/ICCAIS.2015.7338662.
- Torlig, E.M., Alexiou, E., Fonseca, T.A., de Queiroz, R.L., Ebrahimi, T., 2018. A novel methodology for quality assessment of voxelized point clouds. In: Proc. SPIE, 2018. doi:10.1117/12.322741.
- Uchida, T., Hasegawa, K., Li, L., Adachi, M., Yamaguchi, H., Thufail, F.I., Riyanto, S., Okamoto, A., Tanaka, S., 2020. Noise-robust transparent visualization of large-scale point clouds acquired by laser scanning. *ISPRS J. Photogramm. Remote Sens.* 161, 124–134. <https://doi.org/10.1016/j.isprsjprs.2020.01.004>.
- Vahid, S., Wang, S., 2019. Web-based visualization of 3D factory layout from hybrid modeling of CAD and point cloud on virtual globe DTX solution. *Comput. Aid. Des. Appl.* 16, 243–255. <https://doi.org/10.14733/cadaps.2019.243-255>.
- van Oosterom, P., Martinez-Rubi, O., Ivanova, M., Horhammer, M., Geringer, D., Ravada, S., Tijssen, T., Kodde, M., Gonçalves, R., 2015. Massive point cloud data management: design, implementation and execution of a point cloud benchmark. *Comput. Graph.* 49, 92–125. <https://doi.org/10.1016/j.cag.2015.01.007>.
- van Oosterom, P., van Oosterom, S., Liu, H., Thompson, R., Meijers, M., Verbree, E., 2022. Organizing and visualizing point clouds with continuous levels of detail. *ISPRS J. Photogramm. Remote Sens.* 194, 119–131. <https://doi.org/10.1016/j.isprsjprs.2022.10.004>.
- Vincke, S., de Lima, R., Bassier, M., Vergauwen, M., 2019. Immersive visualisation of construction site point cloud data, meshes and BIM models in a VR environment using a gaming engine. *ISPRS – Int. Arch. Photogramm. Remote Sens. Spat. Inf. Sci.* XLII-5/W2, 77–83. <https://doi.org/10.5194/isprs-archives-XLII-5-W2-77-2019>.
- Viola, I., Subramanyam, S., Cesar, P., 2020. A color-based objective quality metric for point cloud contents. In: 2020 Twelfth Int. Conf. Qual. Multimed. Exp., pp. 1–6. <https://doi.org/10.1109/QoMEX48832.2020.9123089>.
- Virtanen, J.-P., Daniel, S., Turppa, T., Zhu, L., Julin, A., Hyypää, H., Hyypää, J., 2020. Interactive dense point clouds in a game engine. *ISPRS J. Photogramm. Remote Sens.* 163, 375–389. <https://doi.org/10.1016/j.isprsjprs.2020.03.007>.

- Wade, N.J., 2021. The vision of Helmholtz. *J. Hist. Neurosci.* 30, 405–424. <https://doi.org/10.1080/0964704X.2021.1904182>.
- Wang, Z., Bovik, A.C., Sheikh, H.R., Simoncelli, E.P., 2004. Image quality assessment: from error visibility to structural similarity. *IEEE Trans. Image Process.* 13, 600–612. <https://doi.org/10.1109/TIP.2003.819861>.
- Wang, S., Liu, L., Qu, L., Yu, C., Sun, Y., Gao, F., Dong, J., 2019. Accurate Ulva prolifera regions extraction of UAV images with superpixel and CNNs for ocean environment monitoring. *Neurocomputing.* 348, 158–168. <https://doi.org/10.1016/j.neucom.2018.06.088>.
- Wang, W., Zhang, Y., Ge, G., Jiang, Q., Wang, Y., Hu, L., 2021. A hybrid spatial indexing structure of massive point cloud based on octree and 3D R*-tree. *Appl. Sci.* 11 <https://doi.org/10.3390/app11209581>.
- Weinmann, M., Weinmann, M., 2019. Fusion of hyperspectral, multispectral, color and 3D point cloud information for the semantic interpretation of urban environments. *ISPRS – Int. Arch. Photogramm. Remote Sens. Spat. Inf. Sci.* XLII-2/W13, 1899–1906. <https://doi.org/10.5194/isprs-archives-XLII-2-W13-1899-2019>.
- Weinmann, M., Jutzi, B., Mallet, C., 2013. Feature relevance assessment for the semantic interpretation of 3D point cloud data. *ISPRS Ann. Photogramm. Remote Sens. Spat. Inf. Sci.* II-5/W2, 313–318. <https://doi.org/10.5194/isprsannals-II-5-W2-313-2013>.
- Weinmann, M., Jutzi, B., Hinz, S., Mallet, C., 2015. Semantic point cloud interpretation based on optimal neighborhoods, relevant features and efficient classifiers. *ISPRS J. Photogramm. Remote Sens.* 105 (2015), 286–304. <https://doi.org/10.1016/j.isprsjprs.2015.01.016>.
- Yang, J., Huang, X., 2014. A hybrid spatial index for massive point cloud data management and visualization. *Trans. GIS* 18, 97–108. <https://doi.org/10.1111/tgis.12094>.
- Zhang, L., van Oosterom, P., Liu, H., 2020. Visualization of point cloud models in mobile augmented reality using continuous level of detail method. *Int. Arch. Photogramm. Remote Sens. Spat. Inf. Sci.* XLIV-4/W1-, 167–170. <https://doi.org/10.5194/isprs-archives-XLIV-4-W1-2020-167-2020>.
- Zhang, D., Xian, C., Luo, G., Xiong, Y., Han, C., 2020. DeepAO: efficient screen space ambient occlusion generation via deep network. *IEEE Access.* 8, 64434–64441. <https://doi.org/10.1109/ACCESS.2020.2984771>.
- Zhang, R., Zakhori, A., 2014. Automatic identification of window regions on indoor point clouds using LiDAR and cameras. *IEEE Winter Conf. Appl. Comput. Vis.* 107–114. <https://doi.org/10.1109/WACV.2014.6836112>.